

Excitonic Phase Transitions in MoSe₂/WSe₂ Heterobilayers

Jue Wang¹, Qianhui Shi², En-Min Shih², Lin Zhou^{1,3}, Wenjing Wu¹, Yusong Bai¹, Daniel A. Rhodes⁴, Katayun Barmak⁵, James Hone⁴, Cory R. Dean², X.-Y. Zhu^{1,*}

¹ Department of Chemistry, Columbia University, New York, NY 10027, USA.

² Department of Physics, Columbia University, New York, NY 10027, USA.

³ College of Engineering and Applied Sciences, Nanjing University, 210093, P. R. China.

⁴ Department of Mechanical Engineering, Columbia University, New York, NY 10027, USA.

⁵ Department of Applied Physics and Applied Mathematics, Columbia University, New York, NY 10027, USA.

*email: xyzhu@columbia.edu

Homo- or hetero-junctions of two-dimensional (2D) materials provide unprecedented opportunities for the exploration of quantum phases¹⁻⁵. Among them, heterobilayers of transition metal dichalcogenides (TMDCs) are attractive because they not only inherit the strong Coulomb correlation and valley pseudo spin from constituent monolayers⁶⁻⁹, but also yield long-lived and charge separated interlayer excitons¹⁰⁻¹⁵ to facilitate exciton condensation^{5,16,17}. Moreover, the great band tunability by interlayer twist angle opens the door to a rich spectrum of phenomena, such as moiré exciton lattices¹⁸⁻²¹, topological mosaics^{22,23}, and correlated many-body physics associated with band flattening^{1,2,24}. Here we explore electronic phase transitions of interlayer excitons in the MoSe₂/WSe₂ heterobilayer. We show direct evidence for the Mott transition from an insulating exciton gas to a conducting plasma when excitation density (n_{ex}) is increased above the Mott density, $n_{\text{Mott}} \sim 3 \times 10^{12} \text{ cm}^{-2}$. The upper limit in photo-generated density of charge separated electron/hole plasma is over 10^{14} cm^{-2} , which is within the range for superconductivity demonstrated before in gate-doped TMDCs²⁵⁻²⁸. We use time and space resolved photoluminescence imaging to map excitonic phase transitions and show that diffusivity is a strong function of n_{ex} . As n_{ex} is lowered, the diffusion coefficient decreases by ~ 3 orders of magnitude in the plasma phase, becomes nearly constant in the exciton phase, but further decreases again by one order of magnitude as n_{ex} approaches $\sim 10^{11} \text{ cm}^{-2}$. The latter is consistent with interlayer exciton trapping in periodic potential wells on the moiré landscape^{20,29}. These findings reveal fundamental bounds for potentially achieving different interlayer exciton phases, such as

moiré exciton lattices, exciton condensates, conducting electron/hole plasmas, and superconductors.

In an excitonic system, the mutual screening effect reduces the exciton binding energy with increasing n_{ex} . Above n_{Mott} , the insulating exciton gas is transformed to a conducting non-degenerate electron-hole plasma (n-EHP)³⁰. Further increase in n_{ex} transforms n-EHP to the degenerate EHP; the distinction between the two is the presence of electron-hole Coulomb correlation in the former but not the latter³⁰. In the case of inter-layer excitons in a TMDC heterobilayer, the conducting EHP corresponds to charge separated sheets of electrons and holes across the interface, as is also known in coupled quantum wells^{31,32}. Intuitively, one can take n_{Mott} as the density where the excitons spatially overlap. An alternative definition comes from band renormalization: n_{Mott} corresponds to the n_{ex} when the decrease in bandgap matches the exciton binding energy³³. For excitons in 2D, there is a universal relationship, $a_0 n_{Mott}^{1/2} \approx 0.25$, where a_0 is the exciton radius³⁴. An upper limit in the value of n_{Mott} can be obtained from the disappearance of excitonic resonances in the absorption spectrum¹⁵.

We choose the model system of MoSe₂/WSe₂ heterobilayer, as interlayer excitons^{10–15}, including moiré excitons^{20,21,29}, have been extensively characterized in this system. With the use of high quality monolayers with very low defect density ($< 10^{11} \text{ cm}^{-2}$)³⁵ and BN encapsulation³⁶, intrinsic interlayer exciton lifetimes as long as 10^2 ns and photo-induced carrier density as high as 10^{14} cm^{-2} have been demonstrated in this system¹⁵. The Mott density is calculated to be $n_{Mott} \sim 1.6 \times 10^{12} \text{ cm}^{-2}$ from the universal relationship based on interlayer exciton radii in the MoSe₂/WSe₂ heterobilayer of $a_0 \sim 2 \text{ nm}$ ^{37,38}. Theoretical analysis of the disappearance of excitonic resonance in absorption spectrum gives an upper limit of $n_{Mott} \sim 3 \times 10^{12} \text{ cm}^{-2}$. We use the transfer-stacking technique to produce BN encapsulated MoSe₂/WSe₂ heterobilayers, as detailed elsewhere^{15,29}. Optical microscope images of the two BN-encapsulated MoSe₂/WSe₂ heterobilayer devices are shown in Fig. S1. In photoconductivity measurement (Fig. S1a), the interlayer exciton is optically dark due to a large twist angle ($\Delta\theta > 5^\circ$). In photoluminescence imaging measurements, we use an optically bright MoSe₂/WSe₂ heterobilayer sample (Fig. S1b) with interlayer twist angle $\Delta\theta = 2.6 \pm 0.5^\circ$, as determined by second harmonic generation. All measurements are carried out at sample temperatures of 4 K.

We first probe the Mott insulator-to-metal transition from photoconductivity as a function of photo-excitation density across the Mott density¹⁵, using a four-terminal geometry (Fig. S2). A continuous wave (CW) laser ($h\nu = 2.33$ eV) is used to uniformly illuminate the heterobilayer including contacts to platinum electrodes. Under this condition, a steady state concentration of excitons/carriers forms from a balance between photo-excitation and recombination. Fig. 1 shows the conductivity as a function of photo-excitation density at zero gate voltage; results for non-zero gate voltage are shown in Fig. S3. Conductivity (s) through the MoSe₂/WSe₂ heterobilayer is not measurable for excitation density $n_{e/h} \leq n_{\text{Mott}}$ indicating that carrier density from intrinsic doping level in the high quality monolayers is too low to contribute to measurable conductivity. Above n_{Mott} , the photoconductivity rises rapidly by more than two orders of magnitude as $n_{e/h}$ increases from 4×10^{12} cm⁻² to 6×10^{13} cm⁻². This result provides direct evidence for the insulator-to-metal transition³⁹: at $n_{e/h} < n_{\text{Mott}}$, the electrons and holes are mostly bound as neutral quasiparticles, i.e., interlayer excitons, that resist dissociation by the moderate DC electric field, while at $n_{e/h} > n_{\text{Mott}}$ the system transitions into adjacent sheets of conducting electrons and holes that move in opposite directions under the DC electric field. The photo-excitation density under both pulsed and CW conditions has been discussed before¹⁵ and calibrated here for the optically bright sample, Fig. S4. We assume the same calibration for the heterobilayer sample used in transport measurement.

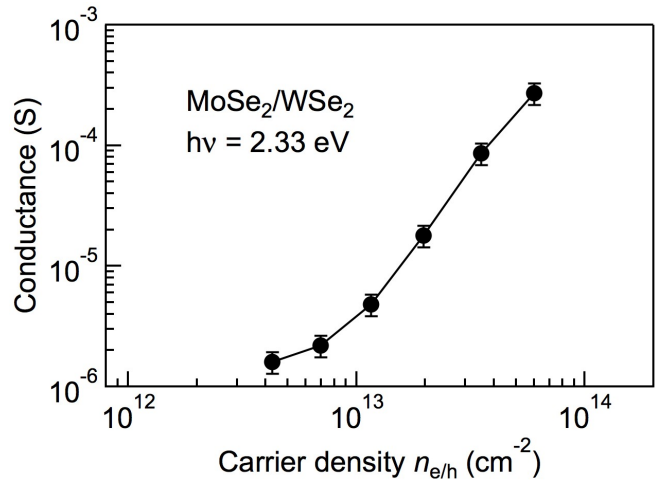


Fig. 1 | Photoconductance of MoSe₂/WSe₂ heterobilayer. Conductivity as a function of photo-excited density showing an insulator state to metal transition. The onset of photoconductivity is close to the Mott density, $n_{\text{Mott}} \sim 1.6\text{-}3 \times 10^{12}$ cm⁻². The measurement was done on a four-terminal MoSe₂/WSe₂ heterobilayer device under CW light illumination at $h\nu = 2.33$ eV.

While the conductivity measurement is limited to the metal phase, both the insulator and the metal phases can be probed in diffusion experiments. Conduction and diffusion are related, in that each is limited by the momentum relaxation time during transport. To measure the diffusion coefficient (D), we photo-excite in a selected region of the heterobilayer and determine the spatial expansion of the interlayer electrons/holes by scanning confocal photoluminescence microscopy.

We rely on the PL emission peak at ~ 1.36 eV from interlayer excitons or charge separated e/h plasmas^{6,15} as a characteristic probe. This measurement can be carried out in time-resolved or steady-state experiments.

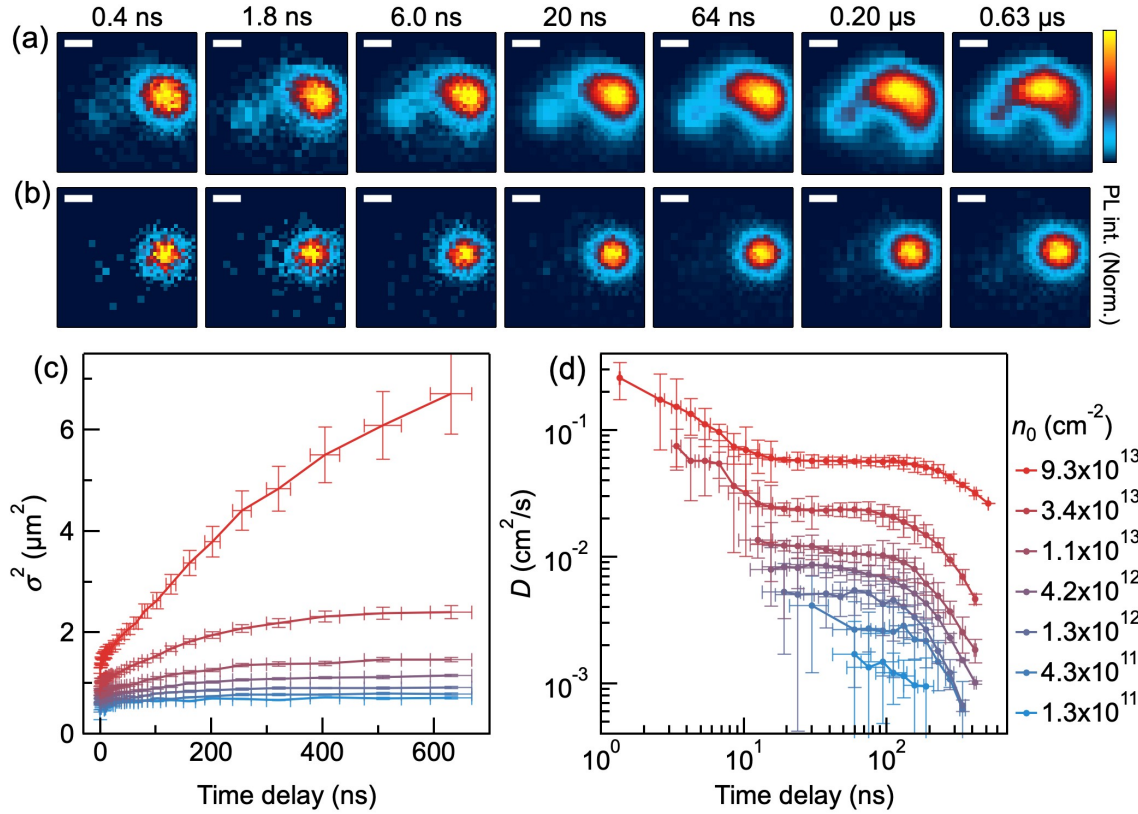


Fig. 2 | Time-resolved diffusion in MoSe₂/WSe₂ heterobilayer. **a, b**, Photoluminescence images at different time delays for high ($9.3 \times 10^{13} \text{ cm}^{-2}$, **a**) and low ($1.3 \times 10^{12} \text{ cm}^{-2}$, **b**) excitation densities. Scale bar, 2 μm . **c**, Spatial variance σ^2 as a function of time at different excitation densities. **d**, Effective diffusion coefficient as a function of time at different excitation densities.

In the time-resolved experiment, we photo-excite a diffraction-limited spot by an ultrafast laser pulse (pulse width ~ 100 fs) and determine the PL intensity with temporal (~ 50 ps) and spatial ($\sim 0.2 \mu\text{m}$) resolution. Fig. 2a and 2b show PL images at different time delays (t) for initial excitation densities of $n_0 = 9.3 \times 10^{13} \text{ cm}^{-2}$ and $n_0 = 1.3 \times 10^{12} \text{ cm}^{-2}$, respectively. Diffusion is reflected in the spatial expansion of PL image with delay time in each case. The PL image expands faster at a higher n_0 in Fig. 2a than it does at a lower n_0 in Fig. 2b. In the former case, the PL image fills the entire heterobilayer region for $t \geq 0.2 \mu\text{s}$; note the presence of a dark region in the lower middle part of the image – see Fig. S5 for complete PL mapping for interlayer exciton emission. We carry out a quantitative analysis of the time-resolved PL images based on the diffusion-reaction equation

with a first order decay term, which has an analytical solution of an expanding Gaussian distribution (see Supporting Information)^{40,41}. We fit the radial profile of the PL image at each time delay to a Gaussian function to obtain $\sigma^2(t)$ at different n_0 values, as detailed in Fig. S6 and Fig. S7. Fig. 2c plots the $\sigma^2(t)$ values as functions of delay time. For each n_0 , the slope of the time-dependent spatial variance gives the diffusion coefficient, D , shown as functions of delay time in Fig. 2d. In the case of high n_0 when the PL image becomes asymmetric and diffusion into the entire heterobilayer region occurs, we carry out analysis of both homogeneous regions and entire images. The resulting time-dependent variances are similar (Fig. S8).

The diffusion coefficient in Fig. 2d is not a constant but depends on t and n_0 . At each n_0 , the carrier density is substantially reduced during the rapid expansion from the diffraction-limited spot ($\sigma_0^2 \approx 0.05 \mu\text{m}^2$) and, in the case of $n_0 > n_{\text{Mott}}$, the expansion leads to the Mott transition spatially. While D generally decreases with increasing time for each starting n_0 , the shape of the $D(t)$ curves reveals two distinct transitions. For $n_0 > n_{\text{Mott}}$, $D(t)$ decreases initially until $t \sim 10^1$ ns, beyond which $D(t)$ becomes nearly a plateau; for $t > 10^2$ ns, $D(t)$ decreases again. The first step is associated with the Mott transition, as the highly diffusive e/h plasma phase transitions to the less diffusive interlayer exciton phase. The excitation density dependence of $D(t)$ in the interlayer exciton phase is found to be weaker than that in the plasma phase. The repulsion among the same charges in each TMDC layer in the charge separated EHP is larger than that among interlayer excitons with inherent dipole moments^{6,10}. The second step occurs within the exciton phase and is characterized by fast decrease in $D(t)$ for $t > 10^2$ ns. This transition becomes invisible only for $n_0 \leq 10^{11} \text{ cm}^{-2}$. The dramatic decrease in the diffusivity of the interlayer excitons in the low density region at long time delays can be attributed to effective trapping. The formation of the MoSe₂/WSe₂ heterojunction results in a moiré potential landscape consisting of quantum-dot or quantum-wire like local potential wells with depth of the order of 10s meV^{20,29}. Trapping of interlayer excitons into the moiré potential wells is expected to drastically reduce diffusivity, as is also seen in recent reports on WS₂/WSe₂ heterobilayers^{42,43}. At sufficiently low n_{ex} , the interlayer excitons become immobile and can be called moiré excitons^{20,22}.

There are three approximations in the above analysis. The first approximation comes from the limited time resolution (~ 0.25 ns) of our PL imaging technique. As a result, significant expansion already occurs in the first PL image frame at high n_0 , beyond the initial diffraction-limited exciton spot. The observed initial spatial variance, $\sigma_0^2(0)$, increases with n_0 , as shown by the initial values

in Fig. 2c. If we take the initial spatial profile of PL image at low excitation densities as an upper limit of the excitation profile, $\sigma_0^2 < 0.6 \mu\text{m}^2$, and the time resolution as an upper limit of expansion time ($\Delta t < 0.25 \text{ ns}$), we estimate a lower bound of the initial diffusion coefficient (D_0) at the highest excitation density ($n_0 \sim 10^{14} \text{ cm}^{-2}$) to be $\sim 15 \text{ cm}^2/\text{s}$, which is two-orders of magnitude higher than the largest measurable D value for the first time step in Fig. 2d. This initial rapid expansion may be a combined effect of ballistic transport and drift due to dipolar repulsion, as reported in coupled quantum wells⁴⁴. This rapid expansion leads to the Mott transition, the tail of which is observed in the drop of effective diffusion coefficient in the $t < 10^1 \text{ ns}$ range, as seen in Fig. 2d. The second approximation comes from fitting the spatial distributions of PL images to Gaussians, with the implicit assumption of a constant diffusion coefficient^{40,41}. Since the diffusion coefficient is not a constant, the obtained $D(t)$ beyond the initial time represents some effective average. This may explain the offsets of diffusion coefficients in the plateau region in Fig. 2d. The third approximation is the assumption of PL intensity being proportional to n_{ex} . The oscillator strength is known to be a constant below n_{Mott} , but decreases with increasing n_{ex} above n_{Mott} by 20-50% for intralayer exciton when n_{ex} reaches $\sim 5 \times 10^{13} \text{ cm}^{-2}$ range¹⁵. We may assume a similar decrease in oscillator strength for the interlayer exciton when n_{ex} is above n_{Mott} . Due to the initial fast expansion and the limited time resolution discussed above, the results shown in Fig. 2 are for n_{ex} close to n_{Mott} even for the highest n_0 measured here. Thus, the assumption of a constant oscillator strength for the interlayer exciton is valid in our measurement.

Complementary evidence for the Mott transition can be found in PL imaging under CW excitation conditions. In this case, the generation, recombination and diffusion of interlayer excitons or EHPs reach a steady state in the heterobilayer. While n_{ex} can reach up to 10^{14} cm^{-2} at the center of the excitation spot¹⁵, it decays away from the center and approaches zero at sufficiently large radial distance. The spatial distribution of carrier density allows probing of different phases by measuring the local PL spectrum, as successfully applied previously in coupled quantum wells⁴⁵. The real space imaging of the Mott transition, Fig. 3a, is enabled by the dependences on excitation density of the peak intensity (I_{PL}), peak width (full-width-at-half-maximum, FWHM), and average peak energy (E_{avg}) of the interlayer exciton change with n_{ex} (Fig. 3b). In particular, The PL emission peak broadens with increasing density, particularly across the Mott transition, as the narrow resonance associated with interlayer exciton resonances is lost as they convert to correlated electron hole plasmas¹⁵. This process is accompanied by blue shift in

average peak energy with increasing carrier density, a result of dipolar repulsion. Note that the exciton Mott transition is close to a smooth second-order phase transition, not a sharp first-order process⁴⁶.

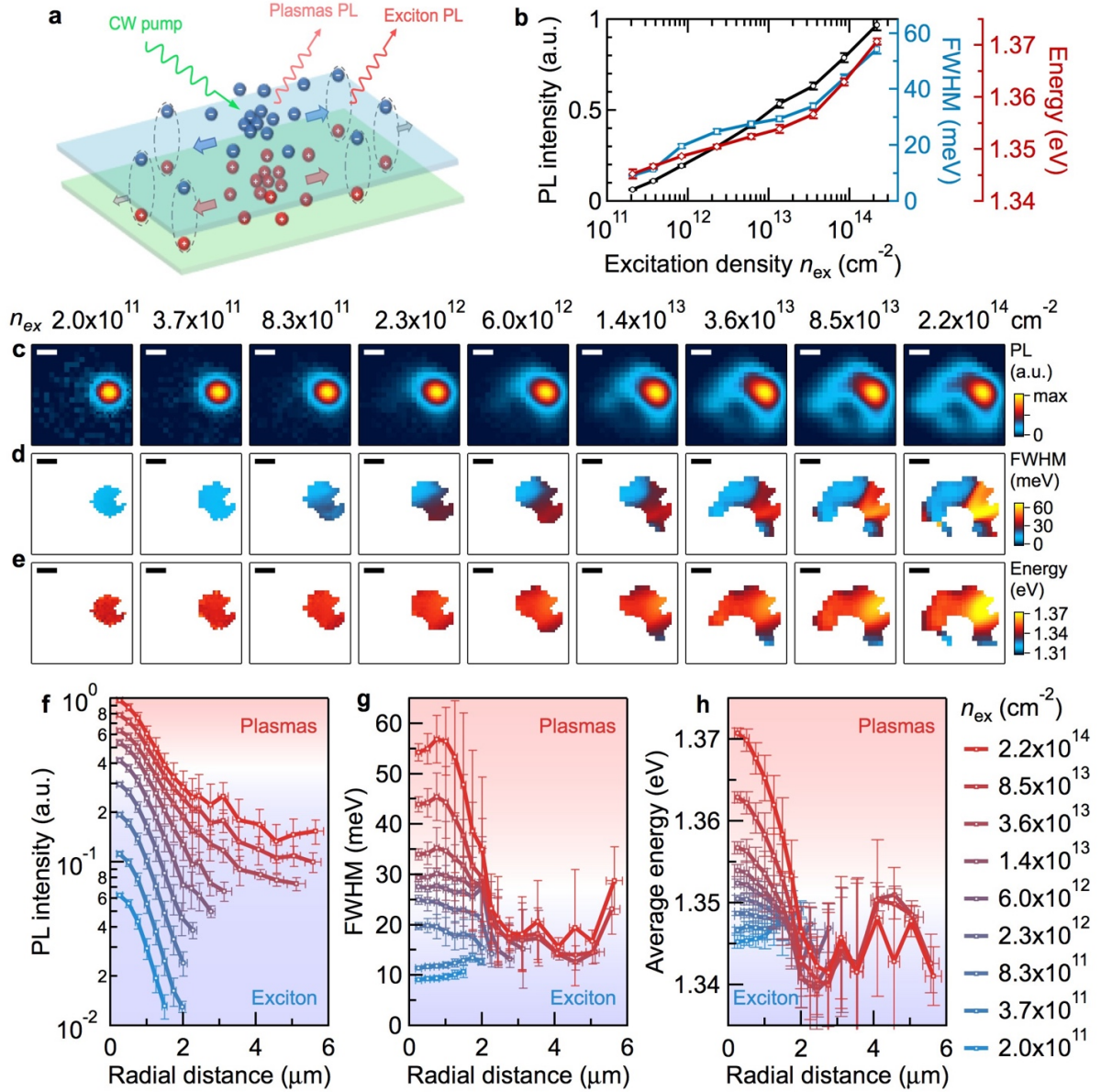


Fig. 3 | Steady-state diffusion in the MoSe₂/WSe₂ heterobilayer. **a**, Schematics showing spatial phase separation in steady-state diffusion experiment. **b**, PL intensity, FWHM and average energy as a function of carrier density at excitation spot. **c**, **d** and **e**, image of PL intensity, FWHM and average energy at different excitation densities, from 2.0×10^{11} cm⁻² (leftmost) to 2.2×10^{14} cm⁻² (rightmost), as listed in the legend of **h**. Scale bar, 2 μ m. **f**, **g** and **h**, PL intensity, FWHM and average energy as a function of radial distance from excitation spot at different excitation densities. The plasmas phase can be seen at high excitation densities within ~ 2 μ m of the excitation spot.

We show spatial maps of I_{PL} (Fig. 3c), FWHM (Fig. 3d), and E_{avg} (Fig. 3e) for a broad range of center excitation densities ($n_c = 2.0 \times 10^{11} - 2.2 \times 10^{14} \text{ cm}^{-2}$). For $n_c < n_{Mott}$, both FWHM and E_{avg} are spatially uniform, consistent with the presence of a single phase of interlayer exciton gas. At center excitation densities well above the Mott threshold, $n_c > n_{Mott}$, the image maps of both FWHM and E_{avg} clearly show spatial gradients that correspond to the e/h plasma phase in the center and the exciton gas phase away from the center. As expected, the e/h plasma phase spatially expands with increasing n_c . We analyze the images quantitatively and show the three quantities as a function of radial distance (ρ) from the center, Fig. 3f, 3g, 3h. The plots of FWHM and E_{avg} clearly reveal a phase boundary at $\rho \sim 2 \text{ }\mu\text{m}$, within which the system is in the e/h plasma phase at $n_c > n_{Mott}$. For $\rho > 2 \text{ }\mu\text{m}$, the system is in the interlayer exciton phase, independent of n_c . From a diffusion length of $l \sim 2 \text{ }\mu\text{m}$ and lifetime of $\tau \sim 20 \text{ ns}$, we estimate a diffusion coefficient of the plasma of $D = l^2/\tau \sim 2 \text{ cm}^2/\text{s}$, which is a reasonable average value for $D \sim 15 - 0.2 \text{ cm}^2/\text{s}$ estimated in time-resolved imaging experiments. Additional analysis can be found in Figs. S10 and S11. Note that the trapped moiré excitons characterized by the exceptionally low diffusivity in the time-dependent measurements in Fig. 2 cannot be resolved in CW imaging experiments in Fig. 3.

The combined photo-conductivity and PL imaging measurements establish the Mott transition around $\sim 3 \times 10^{12} \text{ cm}^{-2}$, from the insulating interlayer exciton gas to the conducting charge separated EHP in the $\text{MoSe}_2/\text{WSe}_2$ heterobilayer. One of the most exciting potentials of excitonic systems is achieving exciton condensation, a macroscopic quantum state bearing similarities to Bose-Einstein condensates (BEC) in cold atom gases. Since the exciton mass is orders of magnitude lower than those of atomic masses, exciton condensation may occur at much higher temperature than a cold atom BEC does. Interlayer excitons in TMDC heterobilayers are thought to be excellent model systems for exciton condensation due to the much increased exciton lifetime and strong manybody correlation in 2D^{5,16,17}. Our findings of the three phases suggests fundamental limits of achieving interlayer exciton condensation in TMDC heterobilayers. On the one hand, the interlayer exciton density needs to be below the Mott density, i.e., $n_{e/h} < 3 \times 10^{12} \text{ cm}^{-2}$, above which destruction of the bosonic quasiparticle occurs due to screening. On the other hand, the interlayer exciton density should be above the threshold $\sim 10^{11} \text{ cm}^{-2}$, below which trapping into the moiré superlattice overcomes the thermodynamic driving force for transition into the BEC like state. Our findings suggest that interlayer exciton condensation in $\text{MoSe}_2/\text{WSe}_2$ heterobilayers may occur in density range of $10^{11} - 3 \times 10^{12} \text{ cm}^{-2}$, in agreement with a recent interpretation of experimental results of

Wang et al.⁵ The lower bound due to moiré exciton trapping may be tunable by the twist angle (see Fig. S11) or differential strain in the TMDC heterobilayer^{20,22,29,47}. The insertion of a BN dielectric layer between the TMDC heterobilayer may substantially reduce or effectively eliminate the moiré traps, thus decreasing the lower bound. This BN sandwich approach has the added advantage of much prolonged interlayer exciton lifetimes for achieving the quasi-equilibrium quantum phase.

In addition to putting constraints on interlayer exciton condensation, our results also reveal limits for two other phases: the moiré exciton lattice at the low n_{ex} limit and superconductivity at the high n_{ex} limit. On the moiré superlattice landscape, interlayer excitons can be trapped into the moiré potential wells to form an ordered exciton lattice which bears resemblance to optical lattice in cold atom physics. Our findings show that such exciton trapping with negligible diffusivity occurs for $n_{\text{ex}} \leq 10^{11} \text{ cm}^{-2}$ in the specific MoSe₂/WSe₂ heterobilayer studied here. This limit is expected from not only the large superlattices but also the inter-exciton screening and repulsion. Thus, when studying moiré exciton physics, one must be mindful that this limit is not exceeded. At the high n_{ex} limit, the charge separated nature of the degenerate EHP means that the sheet of electrons or holes in each TMDC monolayer across the heterojunction is similar to those from gate-doping. Previous measurements of ion-gate doped TMDCs revealed superconductivity at 2D carrier densities in the 10^{14} cm^{-2} range, which is obtainable with our high-quality TMDC heterobilayers under CW light excitation. This raises the tantalizing possibility of achieving CW photo-induced superconductivity in TMDC heterobilayers.

References

1. Cao, Y. *et al.* Correlated insulator behaviour at half-filling in magic-angle graphene superlattices. *Nature* **556**, 80–84 (2018).
2. Cao, Y. *et al.* Unconventional superconductivity in magic-angle graphene superlattices. *Nature* **556**, 43–50 (2018).
3. Li, J. I. A., Taniguchi, T., Watanabe, K., Hone, J. & Dean, C. R. Excitonic superfluid phase in double bilayer graphene. *Nat. Phys.* **13**, 751–756 (2017).
4. Liu, X., Watanabe, K., Taniguchi, T., Halperin, B. I. & Kim, P. Quantum Hall drag of exciton condensate in graphene. *Nat. Phys.* **13**, 746–751 (2017).

5. Wang, Z. *et al.* Evidence of high-temperature exciton condensation in two-dimensional atomic double layers. *Nature* **574**, 76–80 (2019).
6. Rivera, P. *et al.* Valley-polarized exciton dynamics in a 2D semiconductor heterostructure. *Science* **351**, 688–691 (2016).
7. Kim, J. *et al.* Observation of ultralong valley lifetime in WSe₂/MoS₂ heterostructures. *Sci. Adv.* **3**, e1700518 (2017).
8. Jin, C. *et al.* Imaging of pure spin-valley diffusion current in WS₂-WSe₂ heterostructures. *Science* **360**, 893–896 (2018).
9. Rivera, P. *et al.* Interlayer valley excitons in heterobilayers of transition metal dichalcogenides. *Nat. Nanotechnol.* **13**, 1004–1015 (2018).
10. Jauregui, L. A. *et al.* Electrical control of interlayer exciton dynamics in atomically thin heterostructures. *Science* **366**, 870–875 (2019).
11. Hong, X. *et al.* Ultrafast charge transfer in atomically thin MoS₂/WS₂ heterostructures. *Nat. Nanotechnol.* **9**, 682–686 (2014).
12. Rivera, P. *et al.* Observation of long-lived interlayer excitons in monolayer MoSe₂-WSe₂ heterostructures. *Nat. Commun.* **6**, 6242 (2015).
13. Zhu, H. *et al.* Interfacial Charge Transfer Circumventing Momentum Mismatch at Two-Dimensional van der Waals Heterojunctions. *Nano Lett.* **17**, 3591–3598 (2017).
14. Jin, C. *et al.* Ultrafast dynamics in van der Waals heterostructures. *Nat. Nanotechnol.* **13**, 994–1003 (2018).
15. Wang, J. *et al.* Optical generation of high carrier densities in 2D semiconductor heterobilayers. *Sci. Adv.* **5**, eaax0145 (2019).
16. Fogler, M. M., Butov, L. V & Novoselov, K. S. High-temperature superfluidity with indirect excitons in van der Waals heterostructures. *Nat. Commun.* **5**, 4555 (2014).
17. Wu, F. C., Xue, F. & Macdonald, A. H. Theory of two-dimensional spatially indirect equilibrium exciton condensates. *Phys. Rev. B* **92**, 165121 (2015).
18. Jin, C. *et al.* Observation of moiré excitons in WSe₂/WS₂ heterostructure superlattices.

- Nature* **567**, 76–80 (2019).
19. Alexeev, E. M. *et al.* Resonantly hybridized excitons in moiré superlattices in van der Waals heterostructures. *Nature* **567**, 81–86 (2019).
 20. Seyler, K. L. *et al.* Signatures of moiré-trapped valley excitons in MoSe₂ /WSe₂ heterobilayers. *Nature* **567**, 66–70 (2019).
 21. Tran, K. *et al.* Evidence for moiré excitons in van der Waals heterostructures. *Nature* **567**, 71–75 (2019).
 22. Yao, W., Xu, X., Liu, G.-B., Tang, J. & Yu, H. Moiré excitons: From programmable quantum emitter arrays to spin-orbit-coupled artificial lattices. *Sci. Adv.* **3**, e1701696 (2017).
 23. Wu, F., Lovorn, T. & Macdonald, A. H. Topological Exciton Bands in Moiré Heterojunctions. *Phys. Rev. Lett.* **118**, 1–6 (2017).
 24. Bistritzer, R. & MacDonald, A. H. Moiré bands in twisted double-layer graphene. *Proc. Natl. Acad. Sci.* **108**, 12233–12237 (2011).
 25. Li, L. J. *et al.* Controlling many-body states by the electric-field effect in a two-dimensional material. *Nature* **529**, 185–189 (2016).
 26. Saito, Y. *et al.* Superconductivity protected by spin–valley locking in ion-gated MoS₂. *Nat. Phys.* **12**, 144–149 (2015).
 27. Lu, J. M. *et al.* Evidence for two-dimensional Ising superconductivity in gated MoS₂. *Science* **350**, 1353–1357 (2015).
 28. Lu, J. M. *et al.* Full superconducting dome of strong Ising protection in gated monolayer WS₂. *Proc. Natl. Acad. Sci. U. S. A.* **115**, 3551–3556 (2018).
 29. Bai, Y. *et al.* One-Dimensional Moiré Excitons in Transition-Metal Dichalcogenide Heterobilayers. *arXiv Prepr. arXiv1912.06628* (2019).
 30. Klingshirn, C. F. *Semiconductor Optics*. (Springer Berlin Heidelberg, 2012). doi:10.1007/b138175
 31. Stern, M., Garmider, V., Umansky, V. & Bar-Joseph, I. Mott transition of excitons in

- coupled quantum wells. *Phys. Rev. Lett.* **100**, 256402 (2008).
32. Kiršanskė, G. *et al.* Observation of the exciton Mott transition in the photoluminescence of coupled quantum wells. *Phys. Rev. B* **94**, 155438 (2016).
 33. Zimmermann, R. Nonlinear optics and the Mott transition in semiconductors. *Phys. status solidi* **146**, 371–384 (1988).
 34. Meckbach, L., Stroucken, T. & Koch, S. W. Giant excitation induced bandgap renormalization in TMDC monolayers. *Appl. Phys. Lett.* **112**, 061104 (2018).
 35. Edelberg, D. *et al.* Approaching the Intrinsic Limit in Transition Metal Diselenides via Point Defect Control. *Nano Lett.* **19**, 4371–4379 (2019).
 36. Ajayi, O. *et al.* Approaching the Intrinsic Photoluminescence Linewidth in Transition Metal Dichalcogenide Monolayers. *2D Mater.* **4**, 031011 (2017).
 37. Gillen, R. & Maultzsch, J. Interlayer excitons in MoSe₂/WSe₂ heterostructures from first principles. *Phys. Rev. B* **97**, 165306 (2018).
 38. Zhu, X.-Y. *et al.* Charge transfer excitons at van der Waals interfaces. *J. Am. Chem. Soc.* **137**, 8313–8320 (2015).
 39. Asnin, V. M. & Rogachev, A. A. Mott transition in exciton system in Germanium. *JETP Lett.* **7**, 360–362 (1968).
 40. Zhu, T., Snaider, J. M., Yuan, L. & Huang, L. Ultrafast Dynamic Microscopy of Carrier and Exciton Transport. *Annu. Rev. Phys. Chem.* **70**, 219–244 (2019).
 41. Ginsberg, N. S. & Tisdale, W. A. Spatially resolved photogenerated exciton and charge transport in emerging semiconductors. *Annu. Rev. Phys. Chem.* **70**, <https://doi.org/10.1146/annurev-physchem-052516-05> (2020).
 42. Yuan, L. *et al.* Anomalous Interlayer Exciton Diffusion in Twist-Angle-Dependent Moiré Potentials of WS₂-WSe₂ Heterobilayers. *arXiv Prepr. arXiv1910.02869* (2019).
 43. Choi, J. *et al.* Moiré Potential Impedes Interlayer Exciton Diffusion in van der Waals Heterostructures. *arXiv Prepr. arXiv1912.11101* (2019).
 44. Vörös, Z., Balili, R., Snoke, D. W., Pfeiffer, L. & West, K. Long-distance diffusion of

- excitons in double quantum well structures. *Phys. Rev. Lett.* **94**, 226401 (2005).
45. Stern, M. *et al.* Photoluminescence ring formation in coupled quantum wells: Excitonic versus ambipolar diffusion. *Phys. Rev. Lett.* **101**, 257402 (2008).
46. Guerzi, D., Capone, M. & Fabrizio, M. Exciton Mott transition revisited. *Phys. Rev. Mater.* **3**, 54605 (2019).
47. Tong, Q. *et al.* Topological mosaics in moiré superlattices of van der Waals heterobilayers. *Nat. Phys.* **13**, 356–362 (2016).

Acknowledgements

All imaging and spectroscopy experiments were supported by the National Science Foundation (NSF) grant DMR-1809680. Sample preparation was supported by the Center for Precision Assembly of Superstratic and Superatomic Solids, a Materials Science and Engineering Research Center (MRSEC) through NSF grant DMR-1420634. The photoconductivity measurement was supported by the Energy Frontier Research Center of the US Department of Energy grant DE-SC0019443. We thank Hanqing Xiong for help with scanning confocal microscopy, Kenji Watanabe and Takashi Taniguchi for providing h-BN crystals.

Author contributions

X.-Y. Z. and J. W. conceived the idea. Q. S., E.-M. S., L. Z. and W. W. fabricated the devices. DAR, with advices by KB and JH, grew the MoSe₂ and WSe₂ single crystals. J. W., Q. S. and E.-M. S. performed the photoconductivity measurements, with supervision from C.R.D. and X.-Y.Z.; J. W. performed the photoluminescence imaging measurements. J. W. analyzed the data. J. W. and X.-Y. Z. wrote the manuscript with input from all authors. X.-Y. Z. supervised the project.

Competing interests

The authors declare no competing interests.

Methods

Device fabrication. . The WSe₂/MoSe₂ device was built from exfoliated van der Waals materials using a dry transfer method, following three essential steps. First, the hexagonal boron nitride (hBN) and graphite flakes were picked up layer by layer and released on a silicon substrate, to serve as the bottom dielectric and gate. Second, Pt electrodes were evaporated onto the hBN in a Hall bar geometry. Finally, hBN, monolayer MoSe₂ and WSe₂ were picked up layer by layer and released onto the bottom hBN with pre-patterned Pt electrodes. All transfer processes were assisted by Polypropylene Carbonate (PPC) conformally wrapped on a polydimethylsiloxane (PDMS) particle fixed on a glass slide, with picking up temperature about 40 - 50 °C and releasing temperature about 120 - 130 °C, respectively.

Photoconductivity measurements. In photoconductivity measurements, the sample was mounted in a liquid helium optical cryostat (Montana Instruments Fusion/X-Plane) with a 100×, NA 0.75 objective (Zeiss). A continuous wave laser (2.33 eV) was focused to the back aperture of the objective in order to create an evenly distributed light field to excite the whole sample. The conductivity of the sample under photoexcitation was measured in four-probe configuration where the sample was biased by an alternating current (500 nA, 17.7 Hz) and the voltage was measured at the same frequency with a lock-in amplifier (Stanford Research Systems SR830). Keithley 2400 was used to apply DC gate voltage through the graphene back gate.

Photoluminescence imaging measurements. Photoluminescence imaging measurements were performed on a home-built scanning confocal microscope system based on the liquid helium optical cryostat. The sample was at 4 K and under vacuum. The photoluminescence image was Fourier transformed by the objective to the back focal plane. This Fourier plane was then imaged by a 4-f system consisting of a tube lens (Thorlabs TTL200MP) and a scan lens (Thorlabs SL50-CLS2) so that the pivot point was imaged to the center of a dual-axis galvo mirror scanning system. The spatial scanning of the sample was achieved by scanning the angles of the galvo mirrors. The reflected photoluminescence was spatially filtered with a pinhole placed at a conjugate image plane and sent to the detector. In the mapping-type experiments, the laser excitation and photoluminescence detection spot was scanned together with a shared light path; in the diffusion-type experiments, the laser excitation spot was fixed while the photoluminescence was still imaged by scanning.

In the time-resolved measurements, a pulsed laser (2.33 eV, 150 fs) from a visible optical parametric amplifier (Coherent OPA 9450) pumped by a Ti:sapphire regenerative amplifier (Coherent RegA 9050, 250 kHz, 800 nm, 100 fs) was used to inject a spatial and temporal pulse of carriers; a single-photon avalanche photodiode (IDQ ID100-50) and a time-correlated single-photon counting module (bh SPC-130) was used to collect time-resolved photoluminescence traces. The instrument response function has an FWHM of 100 ps resulting in a time resolution of about 20 ps. In the steady-state measurements, a continuous wave laser (2.33 eV) was used; an InGaAs photodiode array (Princeton Instruments PyLoN-IR) was used to collect photoluminescence spectra. The wavelength was calibrated by neon-argon and mercury atomic emission sources (IntelliCal, Princeton Instruments). The intensity was calibrated by a 400 to 1050 nm tungsten halogen lamp (StellarNet SL1-CAL).

Supplementary Information

Excitonic Phase Transitions in MoSe₂/WSe₂ Heterobilayers

Jue Wang¹, Qianhui Shi², En-Min Shih², Lin Zhou^{1,3}, Wenjing Wu¹, Yusong Bai¹, Daniel A. Rhodes⁴, Katayun Barmak⁵, James Hone⁴, Cory R. Dean², X.-Y. Zhu^{1,*}

¹ Department of Chemistry, Columbia University, New York, NY 10027, USA.

² Department of Physics, Columbia University, New York, NY 10027, USA.

³ College of Engineering and Applied Sciences, Nanjing University, 210093, P. R. China.

⁴ Department of Mechanical Engineering, Columbia University, New York, NY 10027, USA.

⁵ Department of Applied Physics and Applied Mathematics, Columbia University, New York, NY 10027, USA.

*email: xyzhu@columbia.edu

S1. The samples.

Two h-BN encapsulated MoSe₂/WSe₂ heterobilayer samples were used in the experiments. The first is prepared with Pt electrode contacts, Fig. S1-a. The second is used in PL imaging experiments. The twist angle between the MoSe₂ and WSe₂ monolayers is $\Delta\theta = 2.6 \pm 0.5^\circ$. This same sample has been characterized before (see Fig. S8 in ref. 29)¹.

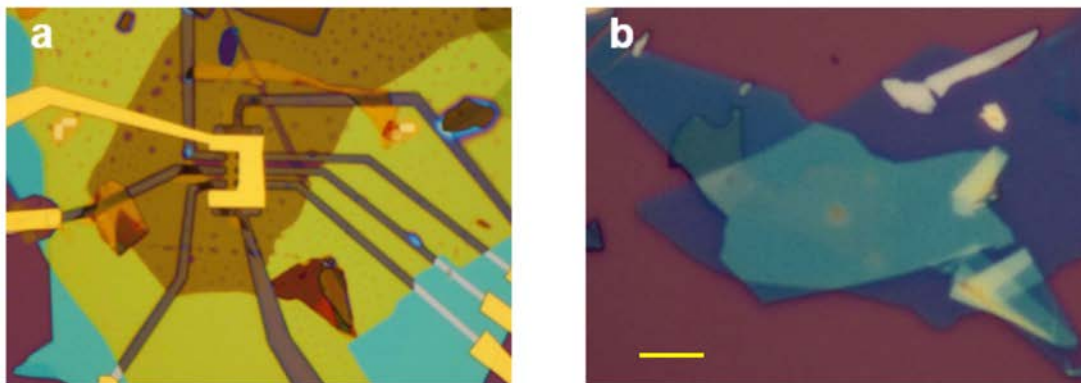


Fig. S1. MoSe₂/WSe₂ heterobilayer samples. Optical microscope images of the sample used in (a) photoconductivity experiments and (b) diffusion experiments. The scale bar (in b) is 5 μm .

S2. Transport measurement

We carried out conductance measurement using a non-ideal geometry due to the different contact resistances of the different metal leads. We tried different combinations and found the configuration shown in Fig. S2 allowed us to carry out reliable measurements with constant current

bias through the source and the drain, and consistent phases on the voltage probes. As shown in Fig. 1 in the main text, we detect non-zero conductance only at excitation densities $\geq 3 \times 10^{12} \text{ cm}^{-2}$. The presence of sufficiently high photocarriers at or above the Mott transition not only provides conducting carriers, but also turns on the contacts. The results shown in Fig. 1 in the main text are obtained from zero gate bias. We have also carried out photoconductance measurements at finite gate biases. Within the range of gate biases, the conductance comes mainly from photodoping and gate-doping only has minor effects.

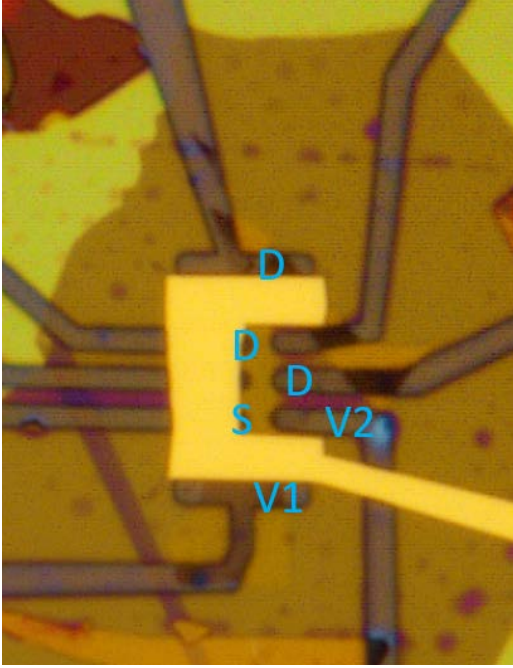


Fig. S2. The transport device, with electrodes marked on the optical image. S: source; D: drain; V1 & V2: voltage probes.

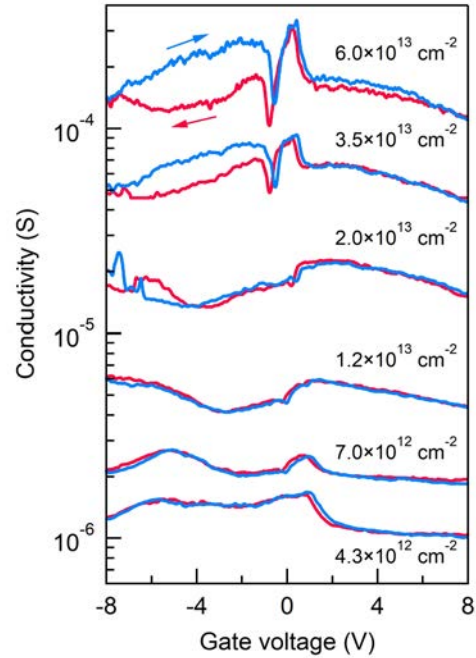


Fig. S3. Gate voltage dependence of photoconductivity at different steady-state excitation densities. Gate sweeping with increasing (decreasing) gate voltage is shown as blue (red) curve in each case.

S1. Diffusion-reaction equation

The diffusion-reaction equation with a first order decay term

$$\frac{\partial n}{\partial t} = D \nabla^2 n - \frac{n}{\tau}$$

where n is carrier density, t is time, D is diffusion coefficient and τ is the decay time constant can be solved by Fourier transforming into the momentum space:

$$\frac{\partial \tilde{n}}{\partial t} = -D\mathbf{k}^2 \tilde{n} - \frac{\tilde{n}}{\tau}$$

where $\tilde{n}(\mathbf{k}, t)$, the Fourier transform of $n(\mathbf{r}, t)$, is

$$\tilde{n}(\mathbf{k}, t) = \tilde{n}(\mathbf{k}, 0) \exp(-Dt\mathbf{k}^2) \exp\left(-\frac{t}{\tau}\right)$$

The inverse Fourier transform then gives

$$n(\mathbf{r}, t) = n(\mathbf{r}, 0) * \frac{1}{4\pi Dt} \exp\left(-\frac{\mathbf{r}^2}{4Dt}\right) \exp\left(-\frac{t}{\tau}\right)$$

where * denotes convolution. In our time-resolved diffusion experiments, the initial carrier density from photoexcitation can be approximated by a 2D Gaussian distribution:

$$n(\mathbf{r}, 0) = n_0 \exp\left(-\frac{\mathbf{r}^2}{2\sigma_0^2}\right)$$

where $n_0 = n(\mathbf{0}, 0)$ is the peak carrier density at time zero and center of excitation spot, σ_0 is the initial spatial variance. Therefore the final solution is an expanding and decaying Gaussian distribution

$$n(\mathbf{r}, t) = \frac{n_0 \sigma_0^2}{\sigma_0^2 + 2Dt} \exp\left(-\frac{\mathbf{r}^2}{4Dt + 2\sigma_0^2} - \frac{t}{\tau}\right)$$

where the square of spatial variance grows linearly with time:

$$\sigma^2 = 2Dt + \sigma_0^2$$

Assuming that (1) the species of interest is independent of other species, (2) the transport is purely diffusional, i.e. the ballistic or drift mechanism are negligible, (3) the diffusion coefficient is a constant over time and space, (4) the decay term is first order, (5) the initial condition is well described by a Gaussian distribution and (6) the experimental probe is proportional to the carrier density, the diffusion coefficient can be extracted from a linear fitting of the $\sigma^2(t)$ curve.

S3. Supplemental data and analysis

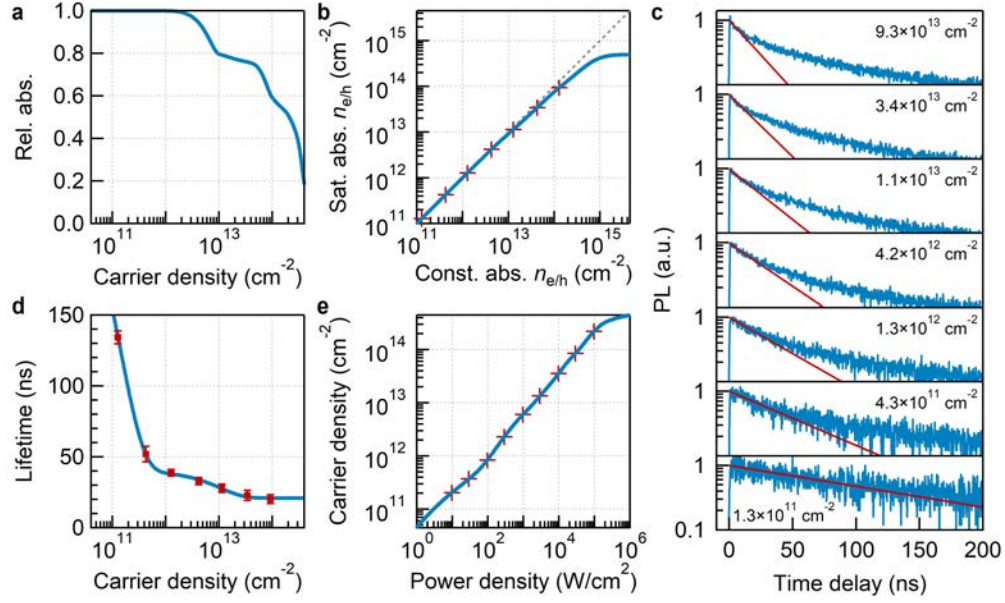


Fig. S4. Calibration of carrier density in MoSe₂/WSe₂ heterobilayers. **a**, Relative absorbance as a function of carrier density showing saturable absorption effect, as obtained from quantum theory². **b**, Calibration of carrier density for pulsed excitation. The actual carrier density considering saturable absorption is plotted against carrier density calculated assuming constant absorption. Red plus sign, the carrier density used in time resolved diffusion experiments. **c**, Time-resolved PL at excitation spot ($r < 0.5 \mu\text{m}$) at different excitation densities. The initial decay was fit by single exponential function shown as red lines. **d**, PL lifetime as a function of carrier density (red squares) and apparent bi-exponential fit (blue lines). **e**, Calibration of carrier density for CW excitation. The steady-state carrier density is plotted against excitation power density. Red plus sign, the carrier density at excitation spot used in steady-state diffusion experiments. The laser photon energies for pulsed and steady-state experiments are both 2.33 eV (532 nm).

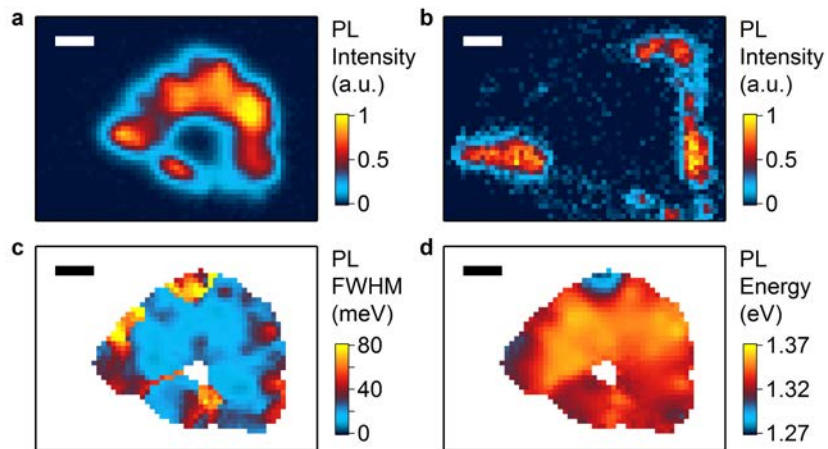


Fig. S5. Photoluminescence image of the MoSe₂/WSe₂ heterobilayer used in diffusion experiments. **a**, Image of interlayer exciton PL intensity. **b**, Image of intralayer exciton PL intensity. **c**, Image of FWHM of interlayer exciton PL. **d**, Image of average energy of interlayer exciton PL. Scale bar, 2 μm .

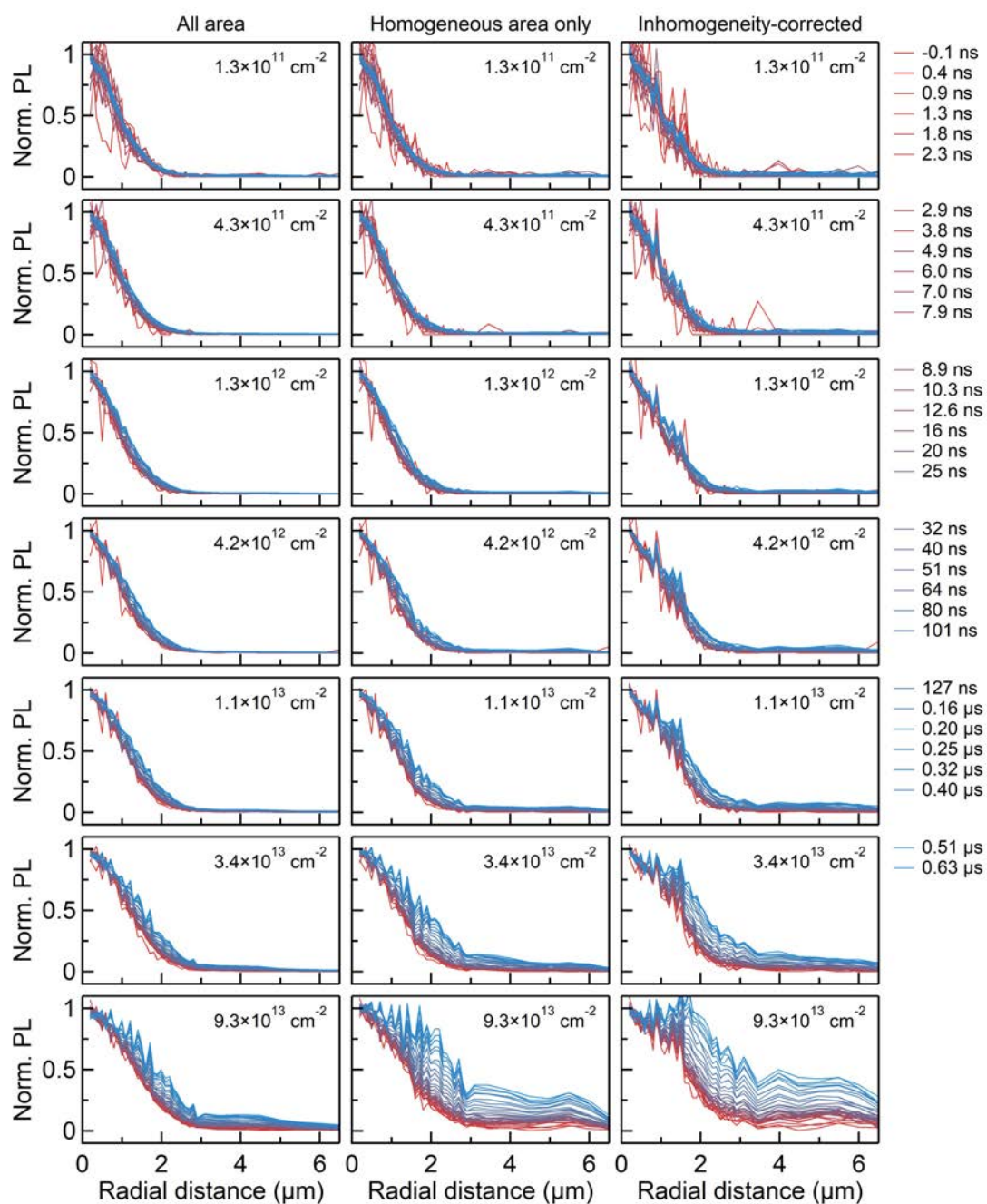


Fig. S6. Evolution of radial PL profile over time. Normalized PL as a function of radial distance and delay time (-0.1 ns to 0.63 μ s from red to blue lines) for different excitation densities (1.3×10^{11} to 9.3×10^{13} cm^{-2} from top to bottom) extracted from time-resolved PL imaging data by three methods (from all area, from homogeneous area only and from inhomogeneity-corrected data, from left to right).

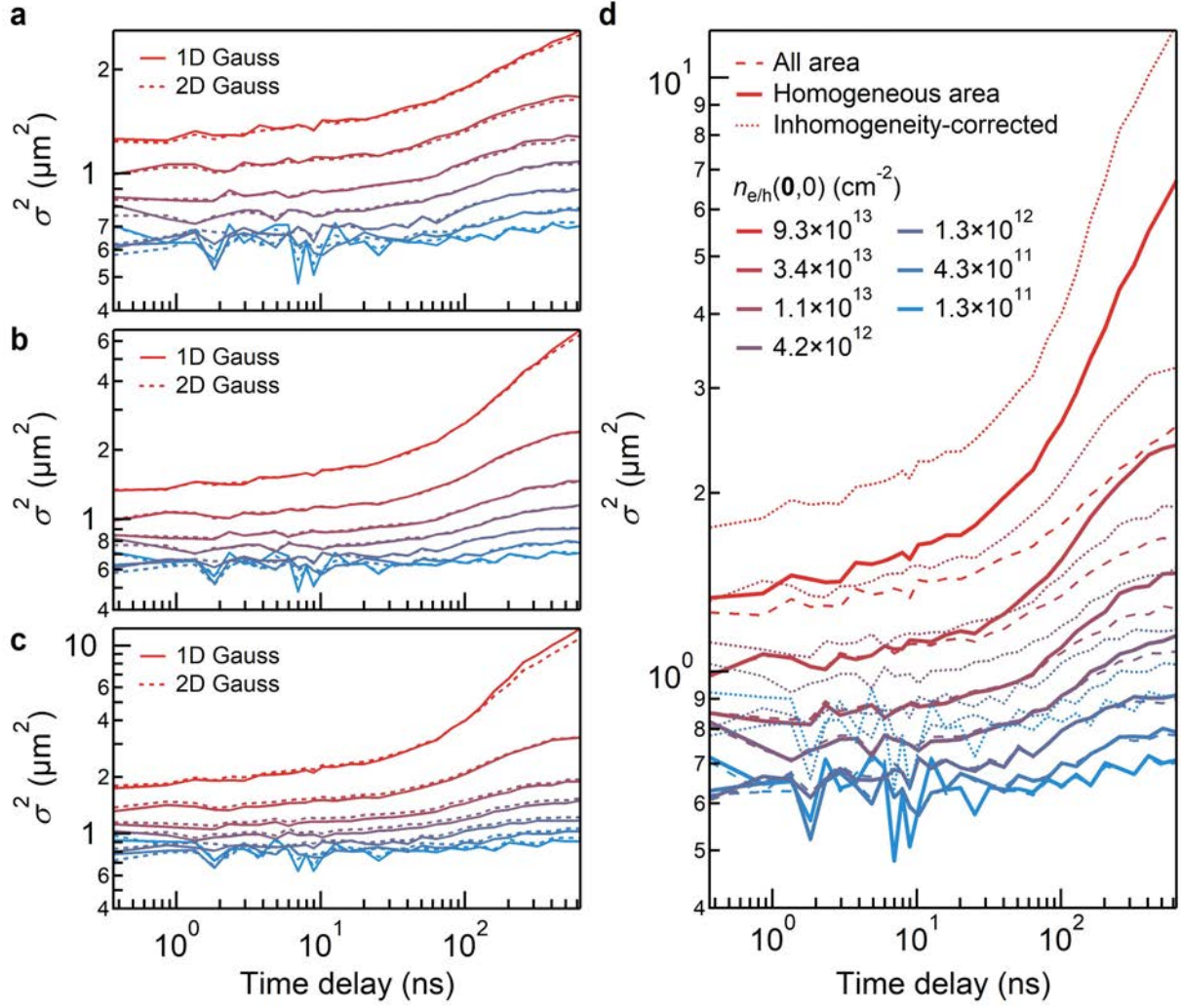


Fig. S7. Comparison of widths extracted by different methods. **a**, Comparison between widths extracted from 2D Gaussian fit to the PL image (dash lines) and from 1D Gaussian fit to the radial PL profile (solid lines), using data from all sample area. **b**, Comparison between 1D and 2D Gaussian widths extracted using data from homogeneous area only. **c**, Comparison between 1D and 2D Gaussian widths extracted from inhomogeneity-corrected data. **d**, Comparison of 1D Gaussian widths extracted from all area, homogeneous area only and inhomogeneity-corrected data. Colors from blue to red indicate different excitation densities $n_{e/h}(0,0)$.

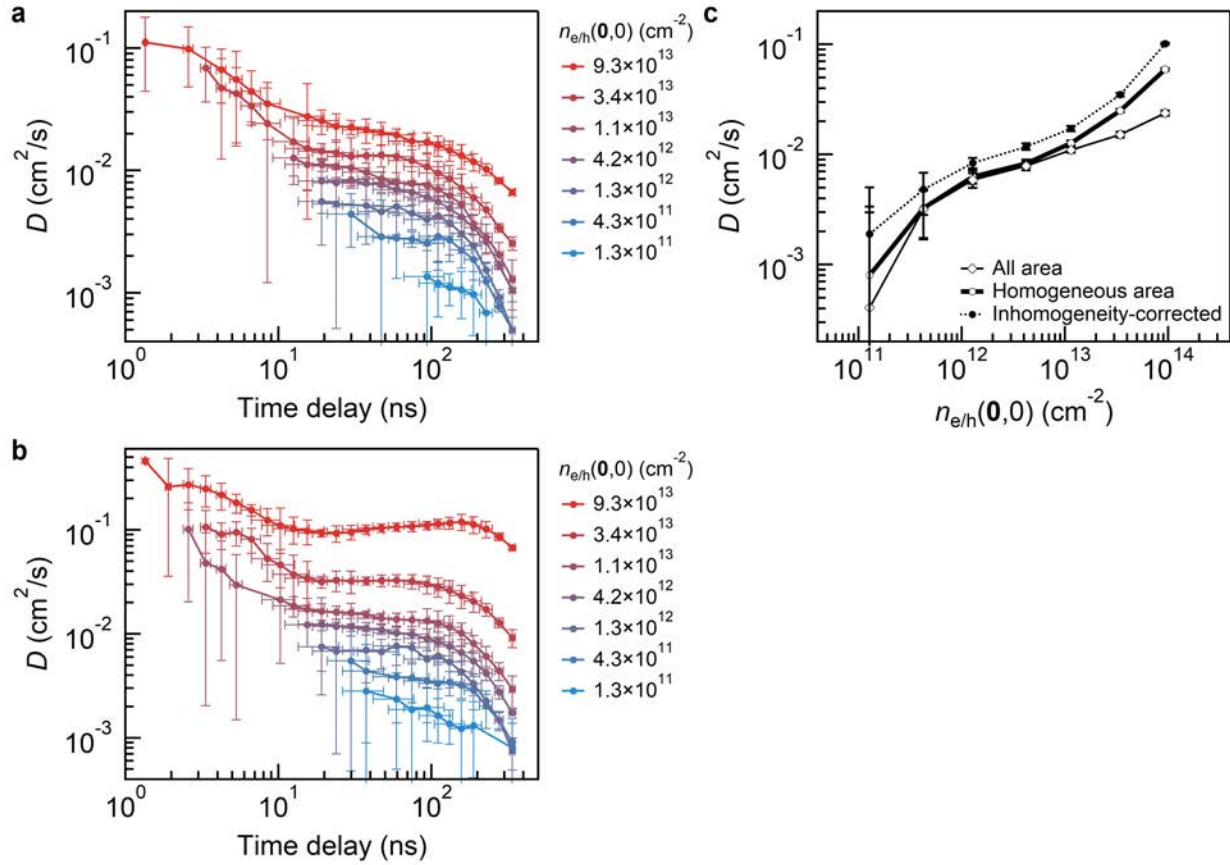


Fig. S8. Comparison of diffusion coefficients extracted by different methods. **a**, Effective diffusion coefficient as a function of time delay and excitation density extracted from image data of all area. **b**, Effective diffusion coefficients extracted from inhomogeneity-corrected image data. **c**, Comparison of plateau diffusion coefficient as a function of excitation density extracted by three methods (from all area, from homogeneous area only and from inhomogeneity-corrected data).

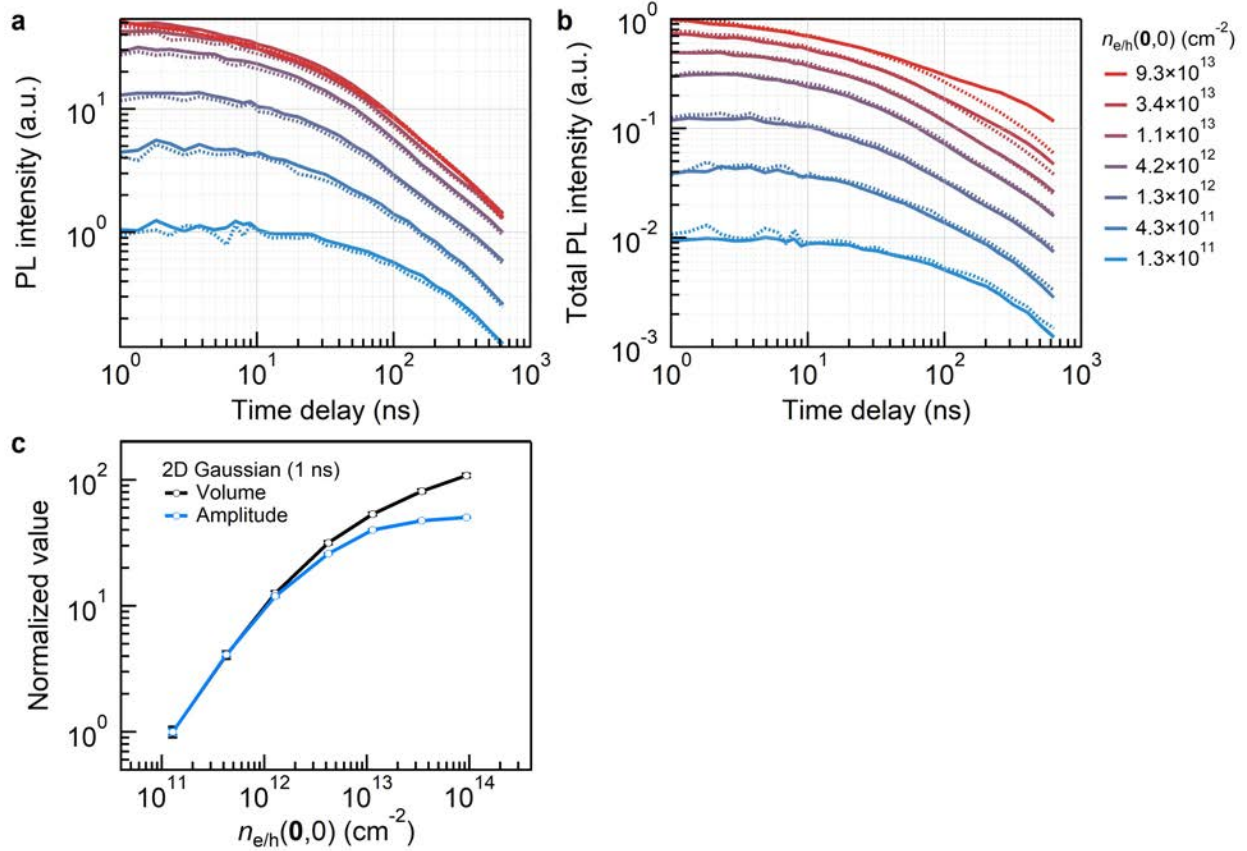


Fig. S9. Photoluminescence decay. **a**, Time resolved PL at center spot ($r < 0.5 \mu\text{m}$, dash lines) or amplitude of 2D Gaussian fit to time resolved PL images (solid lines) at different excitation densities. **b**, Time resolved PL from whole sample (dash lines) or volume of 2D Gaussian fit to time resolved PL images (solid lines) at different excitation densities. **c**, Comparison of excitation density dependence of amplitude and volume of 2D Gaussian fit to PL image at 1 ns delay time.

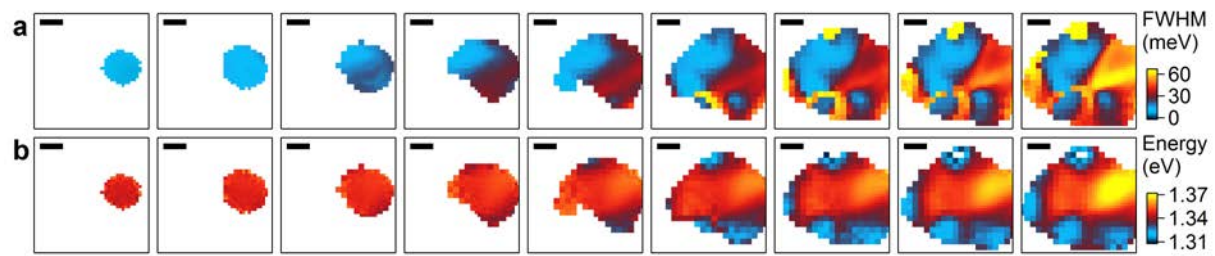


Fig. S10. Photoluminescence characteristics image of steady-state diffusion. **a**, **b**, PL FWHM (**a**) and average energy (**b**) image of steady-state diffusion for carrier densities at excitation spot of 2.0×10^{11} , 3.7×10^{11} , 8.3×10^{11} , 2.3×10^{12} , 6.0×10^{12} , 1.4×10^{13} , 3.6×10^{13} , 8.5×10^{13} and 2.2×10^{14} cm $^{-2}$, from left to right. The FWHM and average energy was extracted from all spots with adequate PL signal, regardless of sample inhomogeneity.

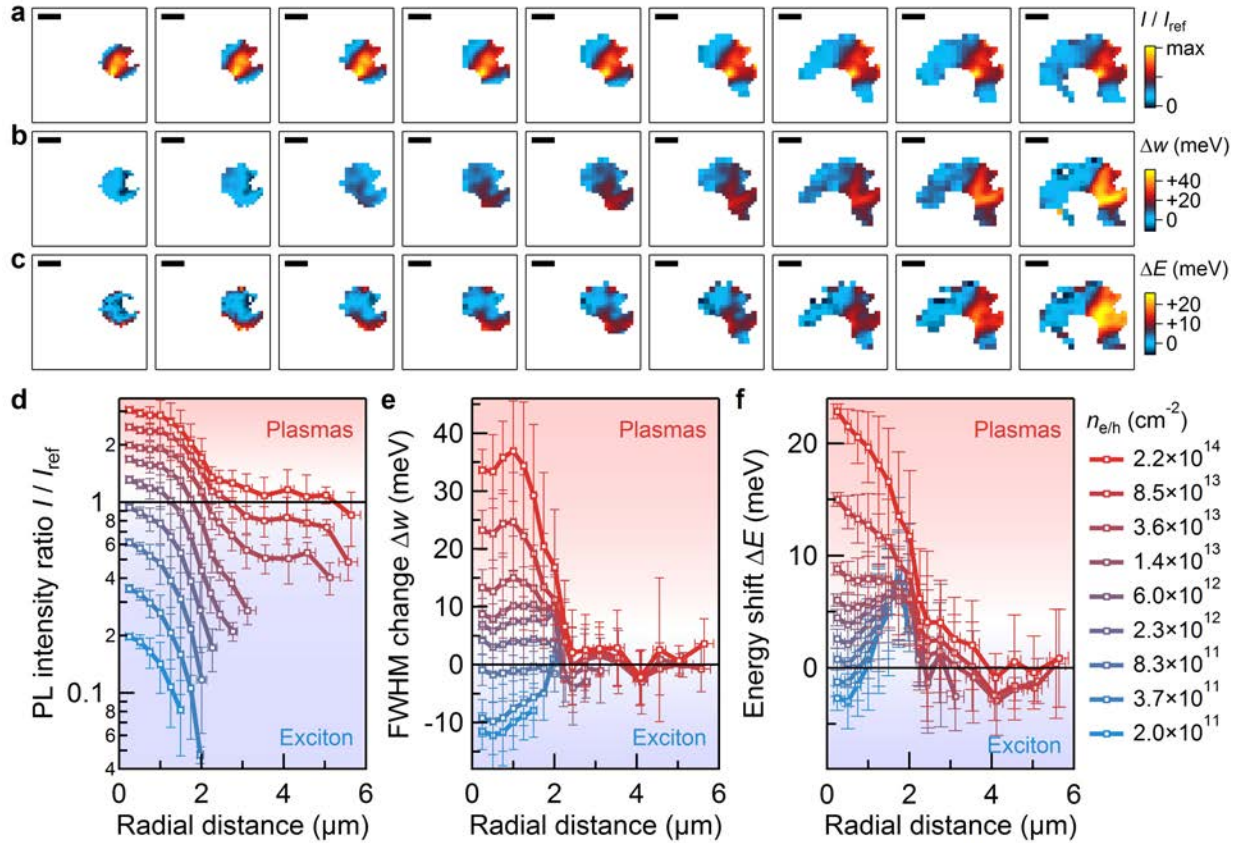


Fig. S11. Inhomogeneity-corrected PL landscape of steady-state diffusion. Similar to Fig. 3 but extracted from inhomogeneity-corrected PL image data. **a, b, c,** The images of PL intensity ratio (**a**), FWHM change (**b**) and average energy shift (**c**) relative to local PL characteristics. The steady-state carrier densities at the excitation spot are 2.0×10^{11} , 3.7×10^{11} , 8.3×10^{11} , 2.3×10^{12} , 6.0×10^{12} , 1.4×10^{13} , 3.6×10^{13} , 8.5×10^{13} and $2.2 \times 10^{14} \text{ cm}^{-2}$, from left to right. **d, e, f,** PL intensity ratio (**d**), FWHM change (**e**) and average energy shift (**f**) as a function of radial distance.

1. Bai, Y. *et al.* One-Dimensional Moiré Excitons in Transition-Metal Dichalcogenide Heterobilayers. *arXiv e-prints* **1912.06628**, (2019).
2. Wang, J. *et al.* Optical generation of high carrier densities in 2D semiconductor heterobilayers. *Sci. Adv.* **5**, eaax0145 (2019).